Original Study   **Open Access**

Bartłomiej Bodak*, Maciej Sobótka

Insights Into Estimation of Sand Permeability: From Empirical Relations to Microstructure-based Methods

Abstract: This study evaluates various methods for estimating soil permeability using microtomography-derived data and compares them to the conventional laboratory approaches. Different methods, including measurement in custom-designed permeameter at micro-CT-compatible scale, empirical equations, simulated sifting, semi-theoretical equations, pore-network modeling, and lattice-Boltzmann simulations, were applied to samples of sandy soils with distinct microstructural properties. The empirical equations showed varied results, highly dependent on the method chosen. The simulated sifting method was able to adequately estimate the granulometric properties of the soil, allowing the use of empirical permeability formulations for substantially small samples. Semi-theoretical equations based on the microstructural properties presented reasonable agreement for some samples. The pore-network modeling approach demonstrated computational efficiency but lacked accuracy. The lattice-Boltzmann method required significant computational resources but did not provide substantially closer alignment with the measured hydraulic properties of some samples. None of the simulations was able to properly determine the permeability of silty and organically contaminated sand. The study highlights the complexity of permeability estimation, emphasizing the need for choosing volumes of interest, resolution of micro-CT scans, and methods that match specific soil characteristics and available computational resources.

Keywords: microtomography; permeability; conductivity; computational fluid dynamics; Kozeny–Carman equation

*Corresponding author: Bartłomiej Bodak, Wrocław University of Science and Technology, Faculty of Civil Engineering,
E-mail: bartlomiej.bodak@pwr.edu.pl
Maciej Sobótka, Wrocław University of Science and Technology, Faculty of Civil Engineering

1 Introduction

Permeability of soil is considered an important parameter in many fields of geotechnical and hydrotechnical engineering. Due to its governing role in flow through porous media, its value is of interest in groundwater analysis, well engineering, material engineering, and fossil fuel industry. The most common form of mathematical definition of permeability is associated with Darcy's equation (Verruijt, 1970):

$$Q = k \frac{A}{\mu L} \cdot \Delta p \tag{1}$$

where Q is the discharge rate [m³/s], k is the absolute permeability [m²], A is the cross-sectional area of the porous medium [m²], μ is the dynamic viscosity [Pa·s], L is the length of the medium [m], and Δp is the difference in pressure between the inlet and outlet of the medium. The above relation applies only to laminar viscous flow at low Reynolds numbers.

In groundwater engineering, assuming the viscosity of the fluid and its temperature constant, hydraulic conductivity can be defined as follows:

$$K = \frac{k \cdot g}{\nu} \tag{2}$$

where K is the hydraulic conductivity [m/s], k is the absolute permeability [m²], g is the gravitational acceleration [m/s²], and ν is the kinematic viscosity [m²/s].

Flow in porous medium is highly dependent on its microstructural properties, jointly included in permeability coefficient as in Eq. (1). It can be acquired by laboratory measurements, tabularized values, correlations with some easy to measure parameters, theoretical microstructure-level models, and direct numerical flow simulations based on identified real microstructure of

the medium. Several empirical and semi-theoretical equations have been developed in attempts to correlate permeability with grain diameter distribution, porosity, compaction factor, specific surface area, and other factors. Some notable examples of empirical formulae are those developed by Hazen (1911), Seelheim (1880), USBR, and Terzaghi (1964), which assume that the flow is mostly dependent on the finest particles in soil composition. Despite their abundant usage, several researchers have found that, in general, this approach may provide mixed results, providing reasonable estimation for some types of soil and significant misestimation for other (Hussain & Nabi, 2016; Pap & Mahler, 2018; Živković et al., 2021).

An alternative approach is adopted in the equations of Kozeny (1927) and Carman (1937, 1956), where the soil is substituted with an equivalent medium that reflects its microstructural properties. However, a significant challenge in applying the above equations lies in the need for accurate estimation of tortuosity and specific surface area, which are not easily obtainable and pose substantial difficulty in acquiring their credible values. In practical applications, these microstructural characteristics have typically been estimated based on empirical assumptions, statistical techniques, or laboratory assessments. Until recently, these parameters made the employing of Kozeny–Carman equations challenging for reliable use in real-world scenarios.

Recent developments in micro-computerized tomography (micro-CT) have revolutionized characterization of porous materials by providing detailed insight into their internal structure, which intrinsically determines their hydraulic properties. This information may be used in two distinct ways: to calculate microstructural properties for use in semi-theoretical permeability estimation methods or to directly simulate fluid flow through the reconstructed medium. Several numerical methods are used to calculate permeability by means of computational fluid dynamics. In the pore-network modeling approach, the geometry of the medium is commonly simplified into a set of one-dimensional elements either by medial axis (Lindquist & Venkatarangan, 1999) or by maximal ball methods (Dong & Blunt, 2009). The direct modeling approach utilizes flow calculation directly in the voxel domain or meshed voxel domain. The most common method of direct simulation is the lattice-Boltzmann method (Frisch et al., 1986).

Nevertheless, the use of modern methods of microstructural characterization is not limited to micro-CT-based approaches. A variety of pore-space imaging techniques are currently available, including, but not limited to, focused ion beams (sequential SEM imaging)

(Blunt et al., 2013), statistical reconstruction based on 2D images of pore-space (Feng et al., 2018; Valsecchi et al., 2020) based on either SEM or optical microscopy, or ^{14}C PMMA impregnation (Kelokaski et al., 2006). These provide a worthy alternative to X-ray tomography, especially beyond the limits of its optimal feature sizes.

The field of soil permeability estimation offers a wide choice of methods, each adopting different assumptions and having its own limitations, while their effectiveness and implementation complexity may vary significantly. Despite the increasing use of micro-CT-based approaches, the proper choice of method for estimation of permeability as an effective alternative for commonly used laboratory measurements remains not trivial. In this paper, various methods of estimating soil permeability based on the data retrieved from micro-tomography are evaluated and their outcomes are compared. Their performance is assessed for three samples of different sandy soils.

The arrangement of the paper is as follows. In the second section, information on samples and their properties and description of utilized methods is provided. Third section contains results of samples reconstruction and calculation of permeability using different techniques of its estimation. In fourth section, results are discussed and the performance of used approaches is compared. In the last section, the conclusions and discussion of further research directions in this topic are presented.

2 Materials and Methods

2.1 Test Samples

The selected soil samples represent three distinctive types of sandy soils. Sample 1, identified as fine sand, exhibits a uniform grain size distribution, sample 2 was characterized as fine sand with traces of lignite, while sample 3 was classified as medium sand, demonstrating a less uniform grain size distribution. The samples were first subjected to macroscopic analysis, measurements of grain size distribution, bulk density, and specific density and falling-head permeability test in oedometer; the latter performed in accordance with the procedure described in EN ISO 17892-11:2019-05. These preliminary laboratory measurements were treated as reference data for this study. All soils were air-dried and in loose state of compaction. The following table summarizes the measured properties of each sample.

Table 1: Measured properties of the samples.

| Sample no.	Sample name	Soil type according to PN-EN ISO 14688-2:2018	Bulk density	Specific density	Porosity in loose state	Hydraulic conductivity in falling-head test at 10°C	Uniformity coefficient $U=d_{60}/d_{10}$	GSD curve slope coefficient $C=d_{30}^2/(d_{60} \cdot d_{10})$
		[-]	ρ [g/cm³]	ρ_s [g/cm³]	φ [-]	K [m/s]	U [-]	C [-]
1	Fine sand	FSa	1.549	2.634	0.412	1.702E-5	1.840	1.054
2	Fine sand with lignite	FSa	1.238	2.644	0.532	3.189E-6	2.532	1.027
3	Medium sand	MSa	1.652	2.654	0.377	4.067E-5	3.147	1.003
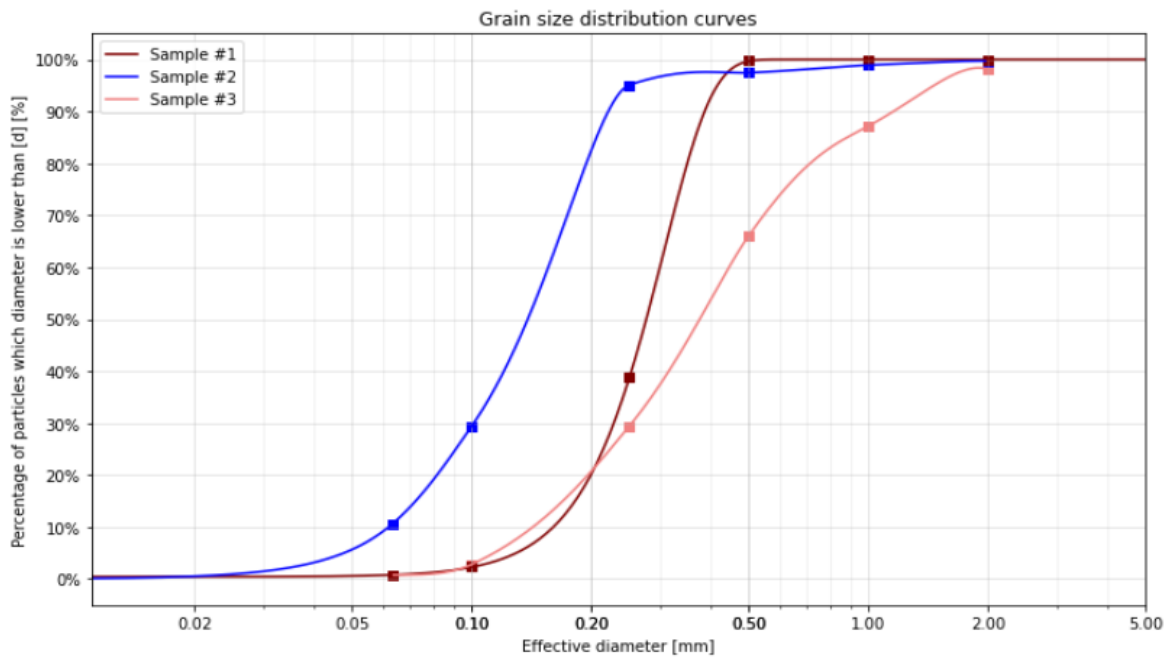
Figure 1: Grain size distribution curves of analyzed samples.

The grain size distribution analysis was conducted according to polish standard PN-EN 933-1:2012. Its results are provided in Figure 1.

2.2 Microcomputerized tomography

In order to acquire microstructure data for analysis, samples were scanned in Bruker Skyscan 1172 system, which consisted of a conical X-ray source with a maximum power of 10 W and 11 MPx CCD image sensor. The first general scan of the whole sample was conducted to accurately measure the length of the soil specimen for permeameter test, utilizing 1 MPx sensor configuration and oversize scanning function. The second scan, utilizing 4 MPx sensor, was to provide microstructure geometry data for further analyses.

3D reconstructions were performed with the NRecon software, which uses Feldkamp algorithm (Feldkamp et al., 1984). Smoothing, misalignment compensation, beam hardening, and ring artifact corrections were further performed to enhance the quality of the reconstructed images. Acquisition and reconstruction parameters were as follows:

- Resolution: 7.8492 µm/px
- X-ray tube voltage: 80 kV
- X-ray tube current: 126 µA
- Filter: Al 0.5 mm
- Angular step: 0.24°
- Smoothing: 1
- Ring correction: 10
- Beam hardening: 30%

2.3 Laboratory approach using the small-scale permeability measurement apparatus

When compared between testing of soil permeability in a falling-head test in oedometer and micro-CT-based imaging methods, a significant challenge arises due to the difference in size of the samples. The inner diameter of the oedometer fixture used in the measurement (50 mm) is significantly larger than the diameter of the sample reconstructed in microtomography (10 mm). The scale effect may lead to problematic interpretation of the resulting permeability values, as the volume of the scanned sample may not be representative in dimensions of the sample in oedometer, and thus, the comparison of both approaches is of questionable validity. To address this challenge and overcome scale discrepancy, a custom unsteady-state permeameter was developed, which is capable of measuring the conductivity of the exact same sample as the one reconstructed in terms of micro-CT.

The core component of this system is a permeameter fixture fabricated using a 3D printing technology. It features a sample holder 10 mm in diameter, as well as inlet and outlet filters. Corrugated wall is incorporated to minimize the influence of boundary flow during testing. Accurate water-level measurement is achieved with the help of custom-made laboratory setup and the use of computer vision (*OpenCV 4.6.0.*, n.d.).

During testing, multiple soil samples are measured simultaneously. The water level as a function of time is later used to fit a theoretical flow curve as in Eq. (3):

$$H(t) = H_0 \cdot exp(-K \cdot \frac{A}{a \cdot L} \cdot (t - t_0)) \qquad (3)$$

where $H(t)$ is a hydraulic height as a function of time [m], H_0 is the hydraulic height during the start of the test [m], A is a sample cross-sectional area [m^2], a is an inlet pipe cross-sectional area [m^2], L is the sample length [m], and t_0 is a parameter accounting for starting time of the test [s].
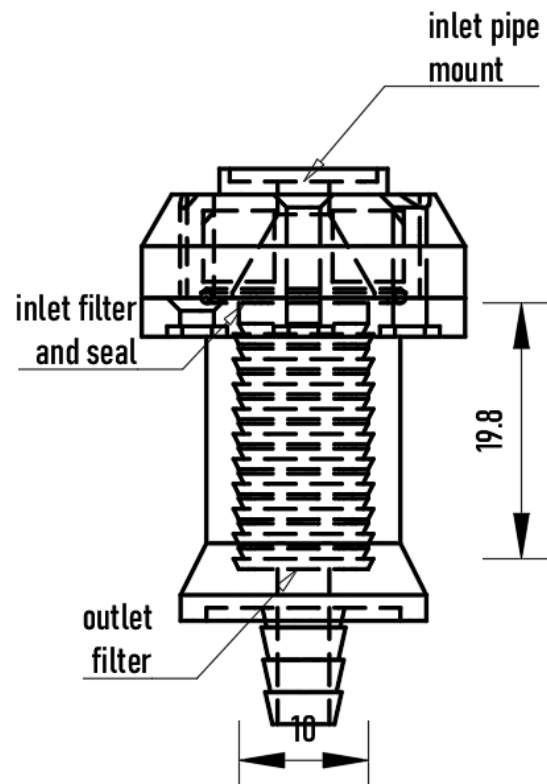

Figure 2: Setup for measurement.

Figure 3: Permeameter fixture.

Table 2: Summary of used empirical formulae.

Method	Equation form	Coefficient C or C'	Porosity function f(φ)	Effective diameter d_e	Exponent m	Applicability
Seelheim (1880)	(5)	3570	1	d_{50}	2	*Sands and clays*
Hazen (1911)	(4)	6.0E-4	$1+10(\varphi-0.26)$	d_{10}	2	*0.1 mm<d_{10}<3 mm* U<5*
Sauerbrey (1932)	(4)	3.75E-3	$\varphi^3/(1-\varphi)^2$	d_{17}	2	*d_{17}<5 mm*
USBR (Říha et al., 2018)	(4)	$4.8E\text{-}4\cdot(1000d_{20})^{0.3}$	1	d_{20}	2	*U<5*
Beyer (1964)	(4)	$6E\text{-}4\cdot log(500/U)$	1	d_{10}	2	*0.06 mm<d_{10}<0.6 mm 1<U<20*
Chapuis et al. (2005)	(5)	1219.9	$\varphi^{2.3475}/(1-\varphi)^{1.565}$	d_{10}	1.565	*0.03 mm<d_{10}<3 mm*

*Due to this limitation, the Hazen equation was not considered valid for sample 2.

Hydraulic height at the start of the test may be adjusted using a regulated outlet overflow. To account for the resistance induced by the apparatus itself, resulting hydraulic conductivity is corrected by the conductivity of permeameter without the soil sample. Measuring setup and permeameter fixture schematic are presented in Figures 2 and 3.

2.4 Empirical methods

In the study, despite their widely known limitations, results of several empirical methods were compared to bridge the gap between commonly used laboratory approaches and micro-CT-based methods. As put together by Vukovic & Soro (1992) and reported by Říha et al. (2018), those equations may be presented in standardized forms (Eq. 4, 5):

$$K = \frac{g}{\nu} \cdot C \cdot f(\varphi) \cdot (d_e)^m \qquad (4)$$

$$K = C' \cdot f(\varphi) \cdot (d_e)^m \qquad (5)$$

where K is the hydraulic conductivity [m/s], g is the gravitational acceleration [m/s²]; C, C', and exponent m are unitless coefficients, f(φ) is a porosity function, and d_e is an effective grain diameter. Values of C, f(φ), m and percentile of grain size used as an effective diameter differ between methods. The equations used, values of coefficients, and applicability conditions are presented in Table 2.

2.5 Methods utilizing microstructure reconstruction in micro-tomography

2.5.1 Simulated sifting method

Accurate results of granulometric analysis play a pivotal role in comprehending the flow characteristics within soil. However, in scenarios where the quantity of soil available for testing is limited or only micro-CT retrieved data are accessible, conventional application of grain size distribution (GSD) measurement faces a significant challenge. In this study, we present a workflow designed to emulate the sieving process through image analysis, allowing for a comparable approach to laboratory tests.

The CT-acquired data were initially subjected to denoising using a nonlocal means filter. Subsequently, threshold values were calculated for each slice of the sample using Otsu's method, and the averaged threshold was used to binarize the entire dataset. The porosity of the resultant binarized arrays was cross-compared with laboratory-obtained porosity values to ensure proper choice of threshold values.

These binarized data arrays were further segmented utilizing the SNOW algorithm (Gostick et al., 2019) to extract point cloud regions corresponding to grains within the analyzed samples. To determine the minimal dimension of the sieve mesh through which each grain could pass, the minimal bounding box (MBB) for each grain was computed. This bounding box essentially forms a cuboid that encloses the region occupied by the grain while minimizing its two smallest dimensions (Blott & Pye, 2007). This was accomplished by identifying a rotated coordinate system in which the variance of point coordinates along one axis is maximized. The second

smallest dimension of that MBB was designated as the effective diameter of the grain.

For each chosen virtual sieve size, a weighted sum of grain volumes by intensity of centroid pixels within each region in the original dataset was calculated, yielding the simulated mass of all grains passing through each sieve. This resulted in obtaining grain size distribution curves similar to ones acquired in the laboratory analysis.

Those simulated curves were employed to calculate hydraulic conductivity in a manner similar to that described in Section 2.4.

2.5.2 Semi-theoretical methods based on microstructure properties

In contrast to purely empirical permeability estimation, Kozeny–Carman equations offer deeper insight into flow characteristics as a consequence of soil microstructure. By combining Darcy's law with the Hagen–Poiseuille equation, considering the soil as an arrangement of parallel capillary tubes with equal diameter (d_t), while also incorporating the notion of tortuosity (τ) as a metric for flow pathway elongation within the porous medium, the Kozeny equation can be deduced as follows (Kaviany, 1995):

$$k = \frac{\varphi \cdot d_t^2}{16 k_k} \tag{6}$$

Here, k [m²] represents the permeability of the medium, φ is the porosity, d_t is the diameter of the single capillary [m], and k_k is the Kozeny constant, which is equal to $k_0 \cdot \tau^2$. k_0 is often given as 2.5 for unconsolidated porous media (Wyllie & Rose, 1950). Introducing the concept of hydraulic diameter leads to the Kozeny–Carman equation, expressed as follows (Dullien, 1979):

$$k = \frac{\varphi}{16 k_k} \cdot \left(\frac{4\varphi}{S \cdot (1 - \varphi)} \right)^2 \tag{7}$$

where S denotes the specific surface area of the pore–grain interface per unit volume [1/m].

The accuracy of the resulting permeability value significantly hinges on the accurate estimation of both tortuosity and specific surface area, which were computed numerically within the present study. The first parameter was determined using PyTrax toolkit (Tranter et al., 2019)

based on random walkers method. This approach involves simulating the movement of virtual particles (walkers) that undergo random displacement steps within the pore space of the medium. A simulation of 20 000 walkers was conducted for 10 000 timesteps each. This led to obtaining mean squared displacements of all walkers for each sample. By comparing resulting values to the mean square displacement of walkers in an obstacle-free space, tortuosity of each dataset was determined.

Each segmented region extracted by the segmentation algorithm described in the previous section was later used to calculate the specific surface area. Boundary points of each point cloud were used to mesh its surface with triangles. With the help of *regionprops3d* algorithm (Gostick et al., 2019), surface areas of individual grains were calculated, enabling the determination of specific surface area of the pore–grain interface per unit volume.

2.5.3 Pore-network model

The pore-network modeling (PNM) approach utilizes an analog of flow in porous medium to the current flow in a random resistor network, as first described by Fatt (1956). Generally, the Hagen–Poiseuille law is employed to calculate the conductance of each one-dimensional capillary (throat) that connect nodes of the network (pores). This simplification of the computational domain allows for the calculation of the total flow rate under given boundary conditions by solving a system of ordinary differential equations, as opposed to directly solving the complex three-dimensional Navier–Stokes equations. The concept of the pore-network and its analogous electric form is shown in Figures 4 and 5.

The network was derived from binarized micro-CT-acquired data using the SNOW2 algorithm (Gostick, 2017; Gostick et al., 2019) that encapsulates all the essential steps for generating the pore-network model compatible with the OpenPNM framework for the flow simulation (Gostick et al., 2016). Following this, the imported network underwent a preprocessing step, which consisted of assessing network integrity, trimming of the disconnected pores that did not contribute to fluid transport, and adding boundary pores at the inlet and outlet planes of samples. Utilizing constant pressure boundary conditions equivalent to a pressure difference of 10 Pa, the subsequent step involved simulating steady-state Stokes flow through the network. The results of the simulation were used to calculate permeability and conductivity using Darcy's law.
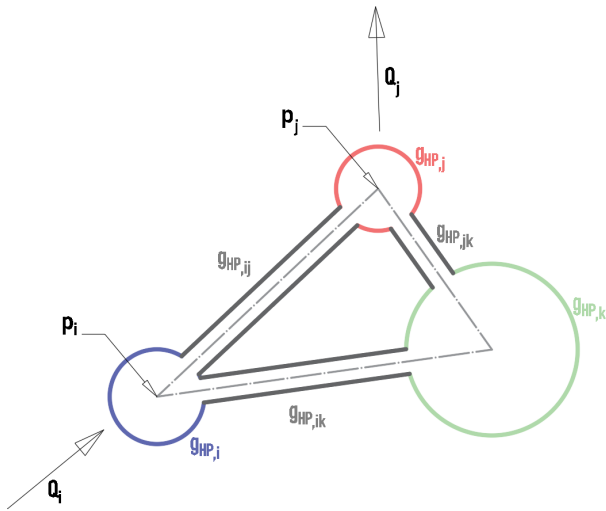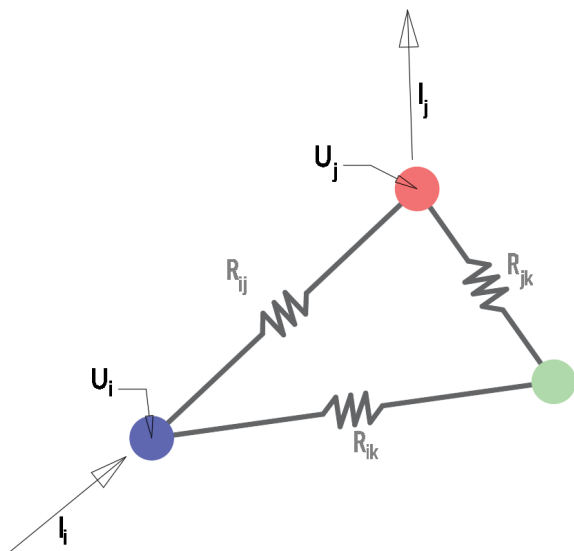
Figure 4: General concept of a pore-network model.

Figure 5: Analogous model of the resistor network.

2.5.4 Lattice-Boltzmann method

The lattice-Boltzmann method (LBM) models fluid particle behavior on a discrete lattice, providing an alternative approach to fluid flow simulation without directly solving Navier–Stokes equations. This method describes flow dynamics in mesoscale, where simulated particle interactions and collisions drive its macroscopic behavior. In contrast to other particle-based methods, LBM places emphasis on monitoring velocity distribution functions at nodes instead of tracking individual particle velocities. By evolving these distribution functions in discrete time steps, LBM simulates the collective behavior of particles on a lattice grid, capturing macroscopic fluid flow dynamics. The 3D LBM solver used in this study (Yang et al., 2022) implements a common model of 19 velocities at each node, often called D3Q19 and multiple-relaxation-time (MRT) scheme to improve its numerical stability and shorten the computation time.

The primary advantage of the LBM is the simplicity of the preprocessing step, as the solver directly operates on binarized data retrieved from micro-CT 3D images. Similar to the PNM approach, constant pressure boundary conditions were applied at inlet and outlet planes, resulting in a pressure difference of 0.005 in lattice pressure units. This corresponded to approximately 1 Pa in SI units considering the predetermined solver parameters. Due to the unsteady nature of flow simulated in LBM solvers, precautions were taken to ensure that the sample's conductivity and permeability were calculated based on the flow rate approaching its asymptotic limit. The resulting velocity field in the sample was used to calculate the total flow rate through the medium, and after conversion from lattice units to SI units (Krüger et al., 2017), permeability and hydraulic conductivity were derived.

3 Results

3.1 Reconstruction of samples' microstructures

Samples were scanned in a FDM-printed fixture later used in laboratory permeability measurements. To mitigate the possibility of soil particles displacing due to high angular acceleration of micro-tomograph holder while scanning, the top cover accommodated a piston providing small compressive force to the sample. Figure 6 shows rendered volumetric data of samples as processed by Bruker CTvox software. Figure 7 shows the process of extracting volumes of interests (VOI) from the retrieved data and their resulting binarized form. VOIs of arbitrarily chosen dimensions of 400^3, 600^3, and 800^3 voxels have been selected to systematically gauge each method's sensitivity to varying VOI sizes.

3.2 Laboratory measurements

The conductivities of the specimens were concurrently measured under consistent environmental conditions. Prior to the final measurement, samples underwent
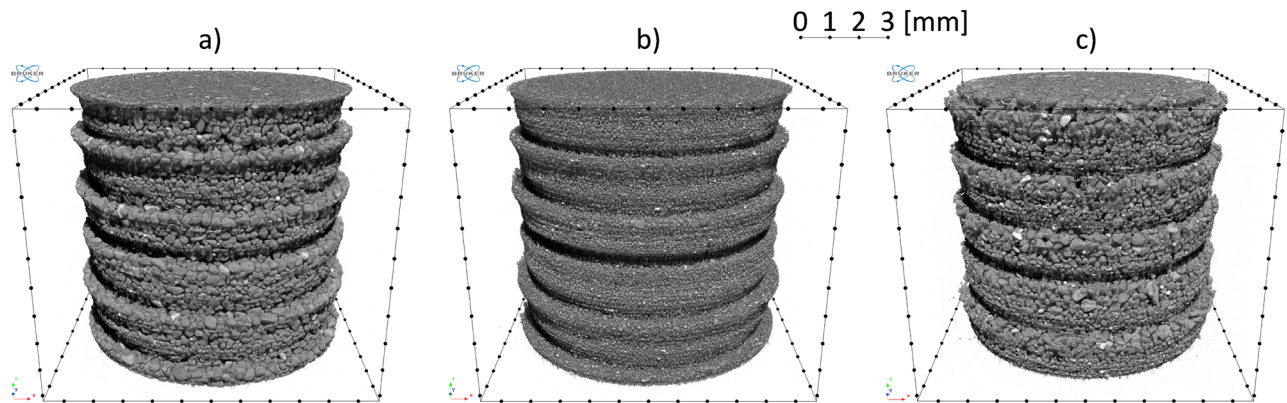
Figure 6: Rendered view of reconstructed a) sample 1, b) sample 2, and c) sample 3.
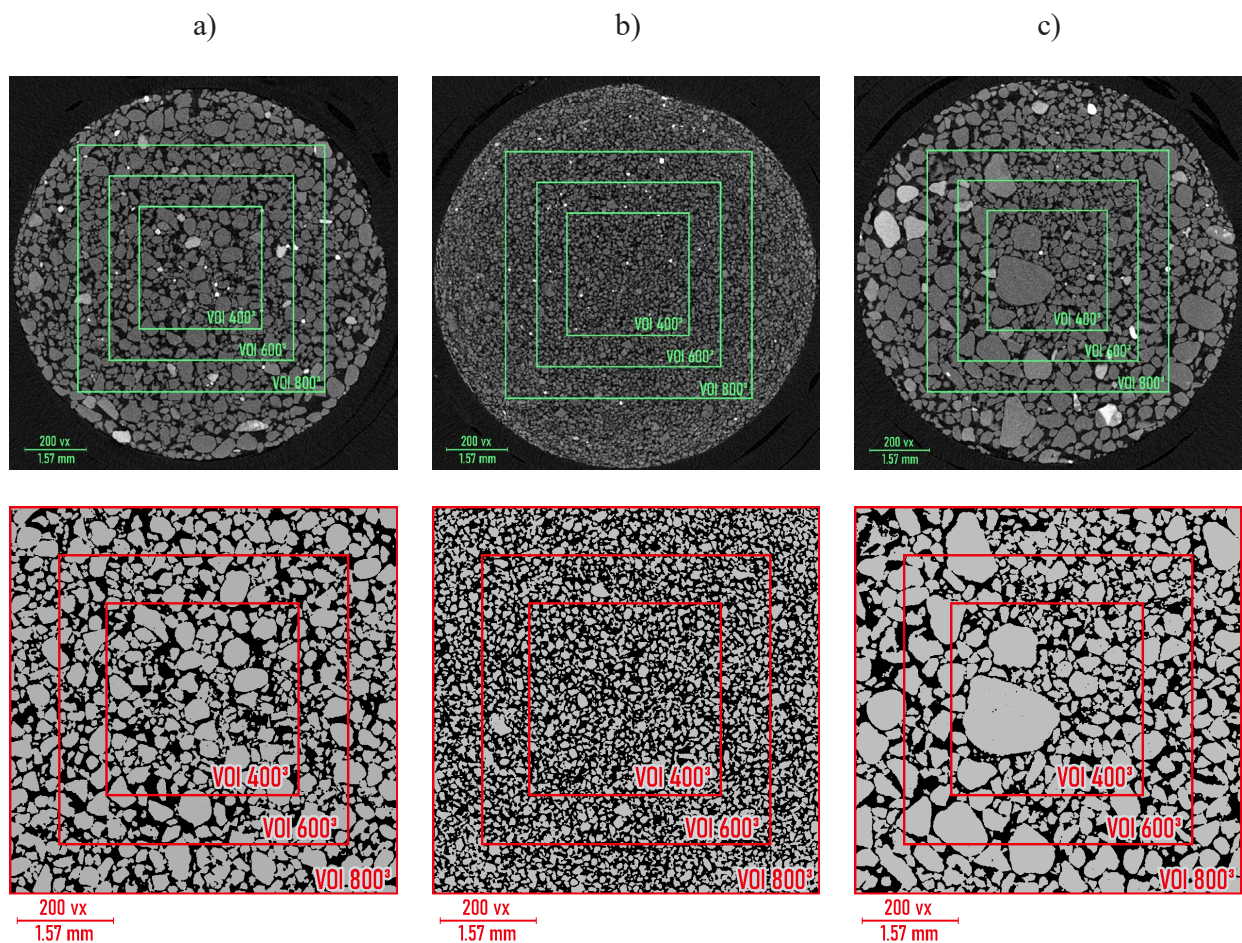

Figure 7: Exemplary slice, volumes of interest and binarized image of a) sample 1, b) sample 2, and c) sample 3.

immersion in water for a duration of 12 h. Subsequently, a series of test runs was conducted under elevated pressure difference to ensure the complete saturation of the soil within the fixture. Raw data acquired with the help of computer-vision-augmented measuring system were subjected to preprocessing to eliminate readings distorted by the pipe holders and erroneous readings. Outcomes of these tests as well as the optimal fits of the theoretical flow curves are depicted in Figure 8.
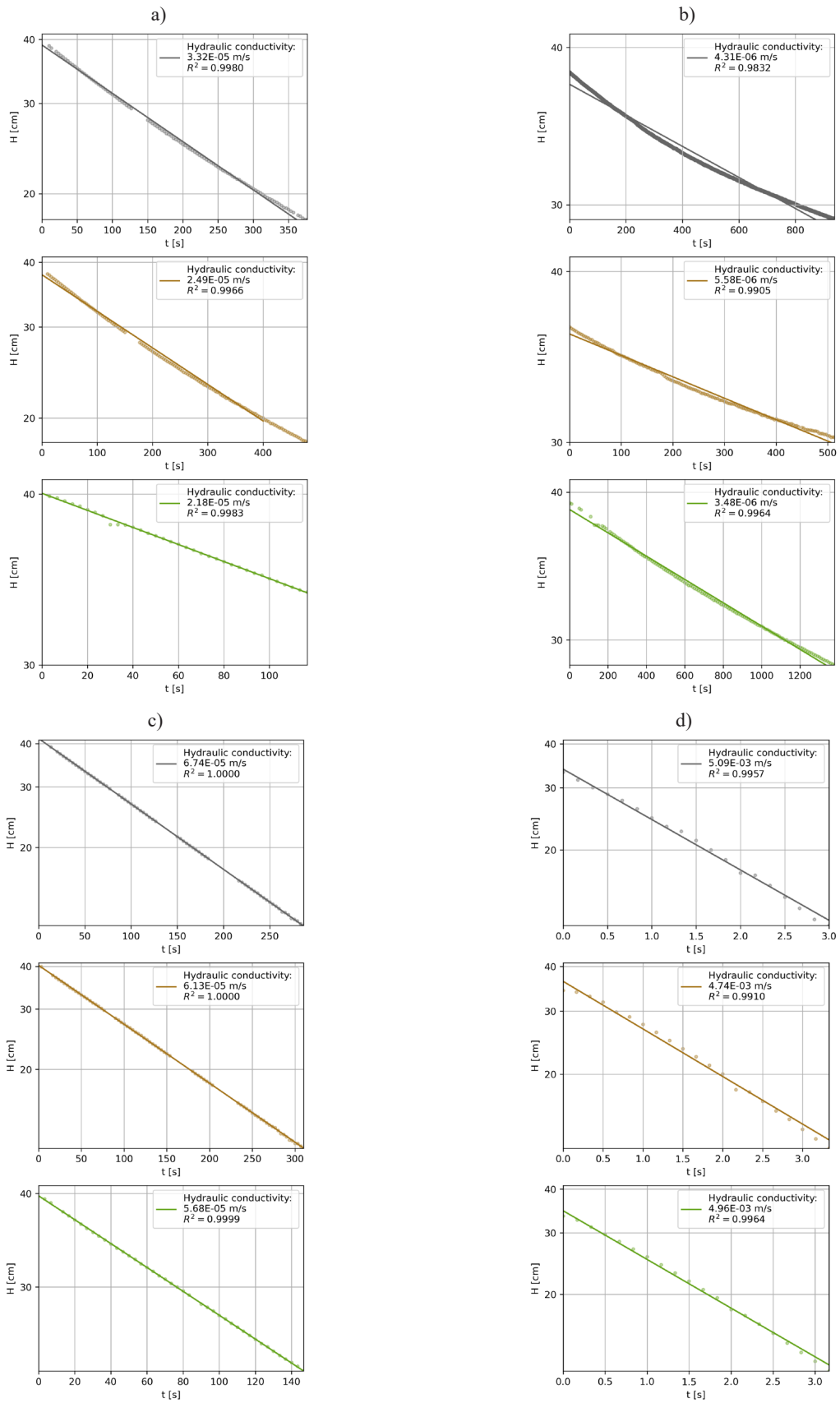
Figure 8: Results of measurements in permeameter and best-fitting theoretical curves: a) sample 1, b) sample 2, and c) sample 3, and d) reference run without the sample attached. The vertical axis is scaled logarithmically for better fitting evaluation.

Table 3: Results of measurements with the described small-scale permeameter setup.

Sample no.	Sample name	Mean conductivity derived from the best-fit curve	Conductivity of the apparatus	Hydraulic conductivity in the measurement temperature	Hydraulic conductivity at 10°C
		K_{equiv} [m/s]	K_{ap} [m/s]	K_{ex} [m/s]	K_{corr} [m/s]
1	Fine sand	2.663E-5	4.927E-3	2.678E-5	1.951E-5
2	Fine sand with lignite	4.457E-6		4.461E-6	3.250E-6
3	Medium sand	6.183E-5		6.262E-5	4.562E-5

The measured hydraulic conductivity values have been corrected to account for the internal flow resistance imposed by the apparatus (i.e. filters) using the following equation (Eq. 8):

$$K_{corr} = \frac{L_{samp}}{\frac{L_{samp}}{K_{meas}} - \frac{L_{ap}}{K_{ap}}} \qquad (8)$$

where L_{samp} is the length of the soil sample measured from the general CT scan [m], K_{meas} is the measured series conductivity of the sample and system [m/s], L_{ap} is the length of the fictional sample, reflecting flow resistance of the measurement setup with no sample attached [m], and K_{ap} is the measured conductivity of the system in the reference test (i.e. without any sample) [m/s]. The results of calculations are depicted in Table 3.

The corrected soil conductivity values obtained through the employed apparatus demonstrated fair coherence with the results of a conventional falling-head test in oedometer. However, they present larger variabilities among individual tests despite similar environmental conditions and constant water temperature. Additionally, observations unveiled that the highly decreasing trend in permeability of sample 2 across successive trials (brown trace in Fig. 8 b) represents the first test, while the green trace denotes the last measured run through the sample, which may indicate influence of swelling, compaction-induced changes in the microstructure of this sample, or filter clogging in the duration of the trial.

Moreover, it is also worth noting that the theoretical curves employed as best-fitting models to the experimental measurements of sample 2 exhibited the worst alignment with the outcomes of the tests. This inconsistency between measured results and theoretical predictions may suggest the need of deeper inquiry into the testing methodology for samples containing larger amounts of silt and organic compounds (i.e., lignite).

3.3 Empirical relations

Hydraulic conductivity of samples was assessed with the use of empirical formulae described in Section 2.4. Effective diameters used for calculations were derived from interpolated values of grain size distribution curves obtained from results of granulometric analysis.

The application of empirically derived formulae to estimate soil conductivity yielded a highly varied range of results as anticipated. Among them, the Seelheim formula stood out by correctly showing that sample 3 had the highest conductivity, while sample 2 had the lowest. The USBR formula in comparison generally provided results that were closest to the actual experimentally acquired values (8.94E-5 m/s, 1.15E-5 m/s, and 8.53E-5 m/s for samples 1–3 accordingly). Beyer, Hazen, Chapuis, and Seelheim formulae have consistently provided overestimated values of conductivity for samples 1 and 3. Interestingly, those formulae (apart from Chapuis formula) have shown smaller error for finely grained sample 2.It is also important to note that there was a significant variation in the results for each sample when different methods were used. This highlights the need for utilizing several distinct formulations when estimating permeability with the use of empirical relations, as the outcomes may vary significantly based on the chosen approach. The resulting conductivity values were summarized in Table 4.

3.4 Simulated sifting

Figure 9 presents grain size distribution curves acquired through the simulated sifting method, contrasting them with the actual grain size distribution curves derived from laboratory granulometric analysis. Figure 10 shows relative differences between hydraulic conductivity values calculated with the use of data from simulated sifting and those from granulometric analysis.

Table 4: Results of estimation using empirical equations.

Sample no.	Sample name	Method	Effective diameter	Effective diameter value	Hydraulic conductivity at 10°C
		[-]	[-]	d_e [mm]	K [m/s]
1	Fine sand	Seelheim	d_{50}	0.273	2.661E-4
		Hazen	d_{10}	0.163	3.031E-4
		Sauerbrey	d_{17}	0.189	2.045E-4
		USBR	d_{20}	0.201	8.937E-5
		Beyer	d_{10}	0.163	2.927E-4
		Chapuis	d_{10}	0.163	4.125E-4
2	Fine sand with lignite	Seelheim	d_{50}	0.138	6.799E-5
		Hazen	d_{10}	0.062	N/A
		Sauerbrey	d_{17}	0.077	1.151E-4
		USBR	d_{20}	0.082	1.150E-5
		Beyer	d_{10}	0.062	3.994E-5
		Chapuis	d_{10}	0.062	2.363E-4
3	Medium sand	Seelheim	d_{50}	0.381	5.182E-4
		Hazen	d_{10}	0.143	2.01E-4
		Sauerbrey	d_{17}	0.179	1.254E-4
		USBR	d_{20}	0.196	8.531E-5
		Beyer	d_{10}	0.143	2.037E-4
		Chapuis	d_{10}	0.143	2.496E-4

The simulated sifting method demonstrated satisfactory outcomes across all three samples. For soils with finer particle compositions (samples 1 and 2), slight differences appeared along the lower part of the grain size distribution curves. This behavior may be attributed to the possible aggregation of finer particles into larger grains, likely arising from intricacies in micro-tomography scanning, reconstruction, and further binarization of the datasets. Despite these differences, the simulated curves provided a satisfactory alignment with the measured values, which was reflected by the high determination coefficients for these samples ($R^2 \geq 0.945$). The magnitude of error can be potentially reduced by fine-tuning the scanning resolution and parameters of the segmentation process for such samples. Notably, expanding the volume of interest did not significantly alter the quality of the results.

For sample 3, characterized by the broader distribution of grain sizes, the method yielded slightly worse results for the overall fitting; however, this reduction was more prominent for the larger sizes of grains. Additionally, expansion of the VOI led to an improvement in a curve alignment, suggesting that the accuracy is impeded by the high size of representative elementary volume or lack of larger grains in scanned sample (given that the physical dimension of VOI at 800^3 voxels roughly corresponds to 6.3 mm in the sample size).

However, it is important to note that for hydraulic conductivity estimation with empirical formulae, greater significance lies in the precise capture of the lower part of the grain size distribution curves, which notably yields best results for sample 3.

3.5 Semi-theoretical method based on microstructure properties

Semi-theoretical permeability estimation in this study was performed using the Kozeny–Carman equation (Eq. 7) and methodology detailed in Section 2.5.2. In contrast to simplified approaches commonly presented (Carrier, 2003; Kaviany, 1995), both tortuosity and specific surface area (SSA) were numerically computed using 3D-image data. The selected number of random walkers in the tortuosity simulation proved to be adequate, as the outcome remained fairly constant with its further
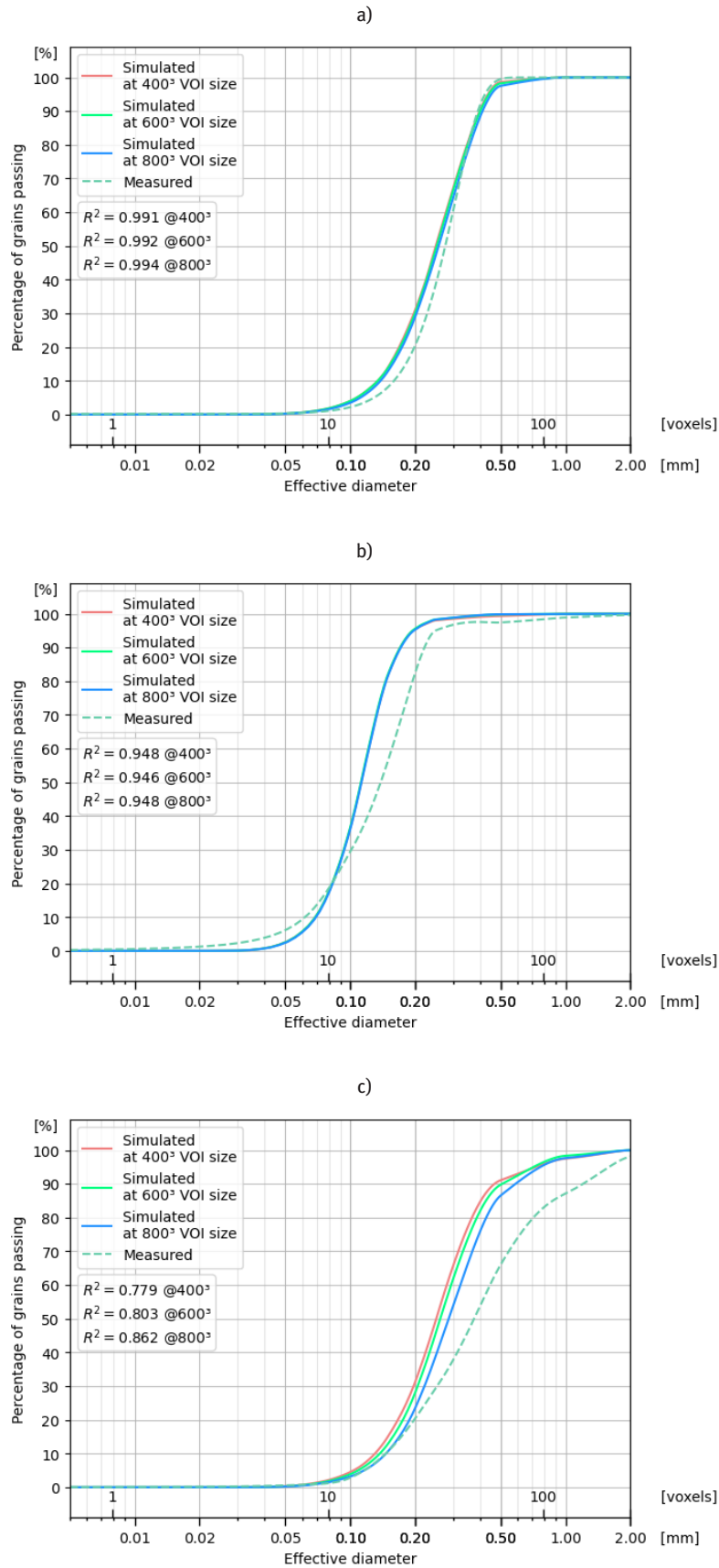
Figure 9: Comparison of measured and simulated grain size distribution curves from different sizes of VOI for a) sample 1, b) sample 2, and c) sample 3.
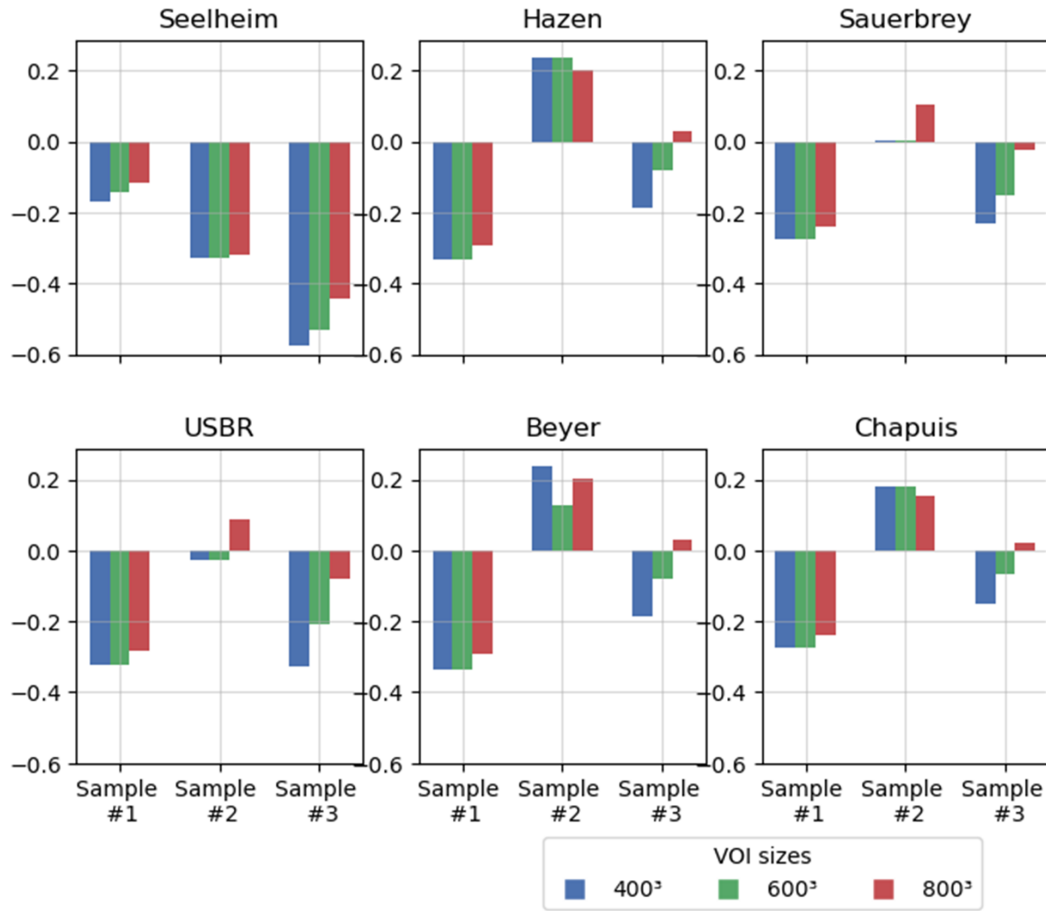
Figure 10: Relative differences between hydraulic conductivity calculated with data from simulated sifting and those from granulometric analysis.
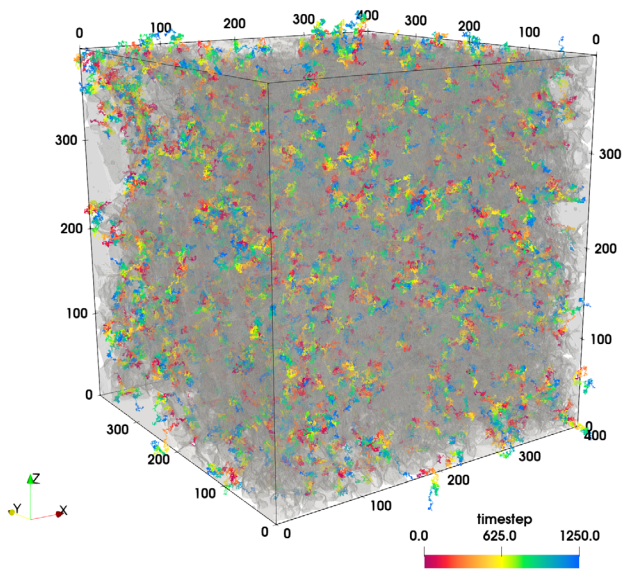

Figure 11: Tracks of random walkers after 1250 time steps in sample 3. Only 10% of all workers are shown for clarity.

increase. An illustrative representation of walkers' trails, acquired with the help of ParaView software (Ahrens et al., 2005), is provided in Figure 11.

In the case of samples 1 and 2, changes in tortuosity and SSA were not notably influenced by the expansion of the VOI extent, leading to relatively stable estimations of conductivity for these samples. However, for sample 3, there was a consistent increase of conductivity as a result of altering the VOI. The summarized outcomes of the described procedure were presented in Table 5.

3.6 Pore-network model

Computations were conducted according to the procedure described in the documentation of the OpenPNM framework (Gostick et al., 2016). Figure 12 (a)-(c) presents rendered pore-network models of samples 1–3 at 400^3 VOI sizes. Each sphere represents a pore-type element, while each tube represents a throat-type element. Color denotes the physical diameter of each element. The flow

Table 5: Results of estimation using the Kozeny–Carman equation.

Sample no.	Sample name	VOI size	Porosity derived from image data	Tortuosity in direction of the flow	Specific surface area per unit volume	Permeability	Hydraulic conductivity at 10ºC
		[vx]	φ_{img} [-]	τ [-]	S [1/m]	k [µm²]	K [m/s]
1	Fine sand	400³	0.365	1.937	38748	16.587	1.242E-4
		600³	0.364	1.935	38447	16.674	1.249E-4
		800³	0.363	1.897	37820	17.378	1.301E-4
2	Fine sand with lignite	400³	0.511	1.732	72321	24.639	1.845E-4
		600³	0.511	1.722	73061	24.283	1.818E-4
		800³	0.506	1.763	72932	22.645	1.696E-4
3	Medium sand	400³	0.309	2.009	40988	7.323	5.484E-4
		600³	0.317	1.980	40043	8.604	6.443E-4
		800³	0.317	1.946	37079	10.209	7.645E-4

Table 6: Results of simulations using the pore-network modeling approach.

Sample no.	Sample name	VOI size	Porosity derived from image data	Permeability	Hydraulic conductivity at 10ºC
		[vx]	φ_{img} [-]	k [µm²]	K [m/s]
1	Fine sand	400³	0.365	23.666	1.786E-4
		600³	0.364	23.587	1.780E-4
		800³	0.363	24.061	1.816E-4
2	Fine sand with lignite	400³	0.511	28.433	2.145E-4
		600³	0.511	27.969	2.110E-4
		800³	0.506	27.338	2.063E-4
3	Medium sand	400³	0.309	17.311	1.306E-4
		600³	0.317	20.301	1.532E-4
		800³	0.317	22.087	1.667E-4

was simulated along the Z-axis of the samples presented here, which was coherent with the flow direction in permeameter. Results of simulations are shown in Table 6.

Extracted pore networks reflected the observed characteristics of each specimen's pore space. However, their topological simplification may be a major factor contributing to the observed overestimation of permeability values, especially for the second sample. This possible reason is supported by comparison of the tortuosity (1.479), specific surface area (62941 1/m), and porosity (0.584) of the network in question with values obtained from image analysis, which reveals substantial discrepancies.

3.7 Lattice-Boltzmann method

In this study, lattice-Boltzmann simulations were conducted using Taichi-lang (Hu et al., 2019) based implementation (Yang et al., 2022). To facilitate high computational demands, a different machine had to be used as LBM is demanding in terms of both CPU/GPU and RAM. Despite its well-recognized suitability for massively parallel computations, the practical applicability of that advantage was hindered by the substantial dimensions of the selected VOI and resolution of the scans. These factors prevented the full harnessing of the parallelism, as the sizes of the samples exceeded what even high-end highly VRAM-equipped GPUs could accommodate –
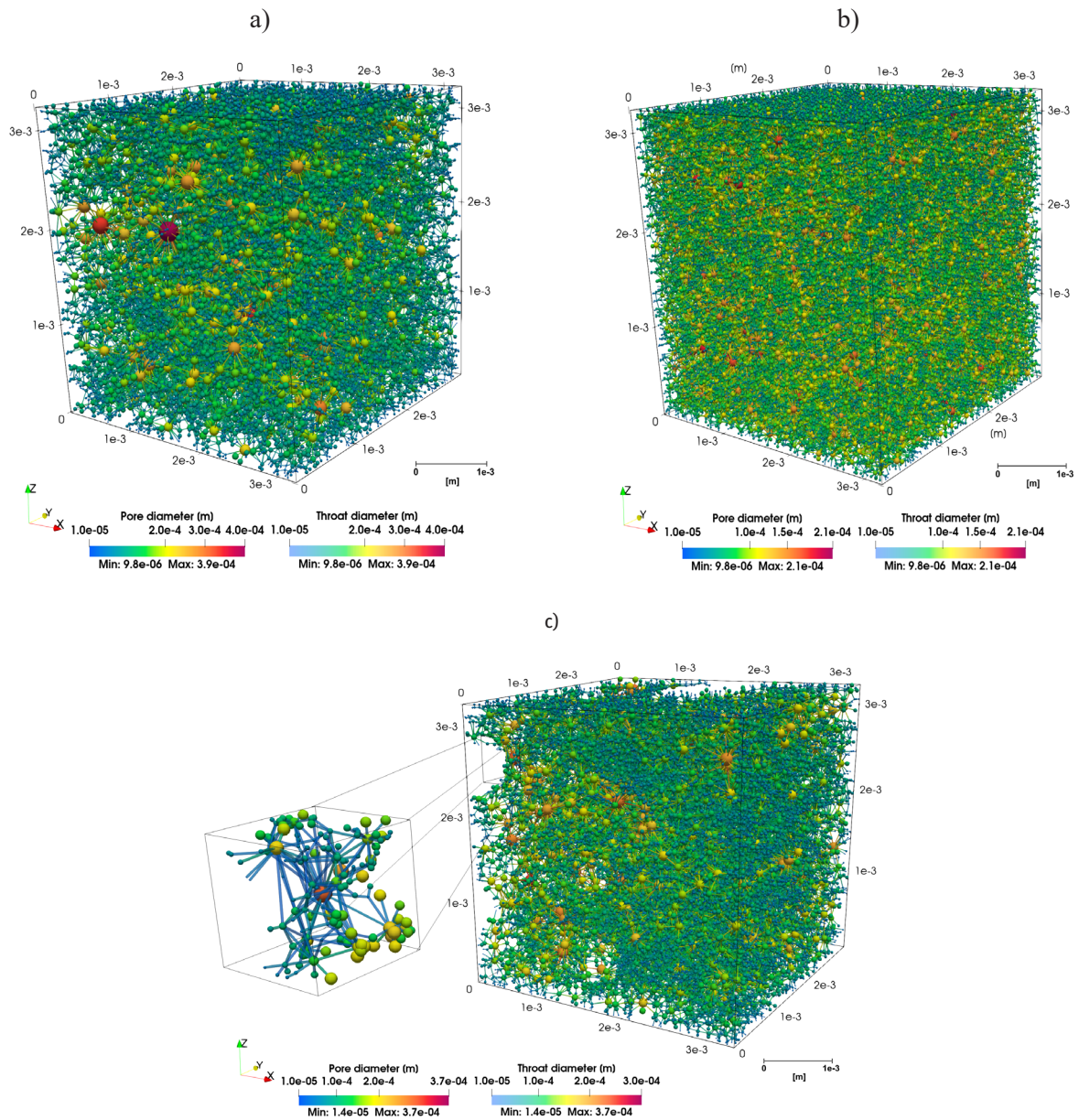
Figure 12: Pore network extracted from a) sample 1, b) sample 2, and c) sample 3 with a zoomed fragment of the network.

such as the Nvidia RTX3090 with 24GB of VRAM, where the practically feasible domain size was found to be constrained to less than 500^3 voxels. Consequently, for the purpose of benchmarking, all simulations were conducted with CPU-based implementation for accurate comparison and evaluation. Even though analyses were made only for 400^3 and 600^3 VOIs, larger sizes would have made the computation impractically long.

Furthermore, it was also observed that the rate of convergence differed not only based on the domain size but also between samples themselves. Sample 2 exhibited the fastest convergence of flow rate toward its asymptotic limit, while sample 1 displayed the slowest. Thus, for accurate results, the flow rate approach to its limit should be closely monitored. Finally, it is worth noting that for samples 1 and 3, the computed permeability values decreased with the increase of the VOI extent, contrary to the behavior of sample 2. Table 7 presents the permeability and conductivity values, as derived from the LBM flow simulation. Figure 13 (a)–(c) depicts streamlines of the flow through the samples.

Table 7: Results of simulations using the lattice-Boltzmann method.

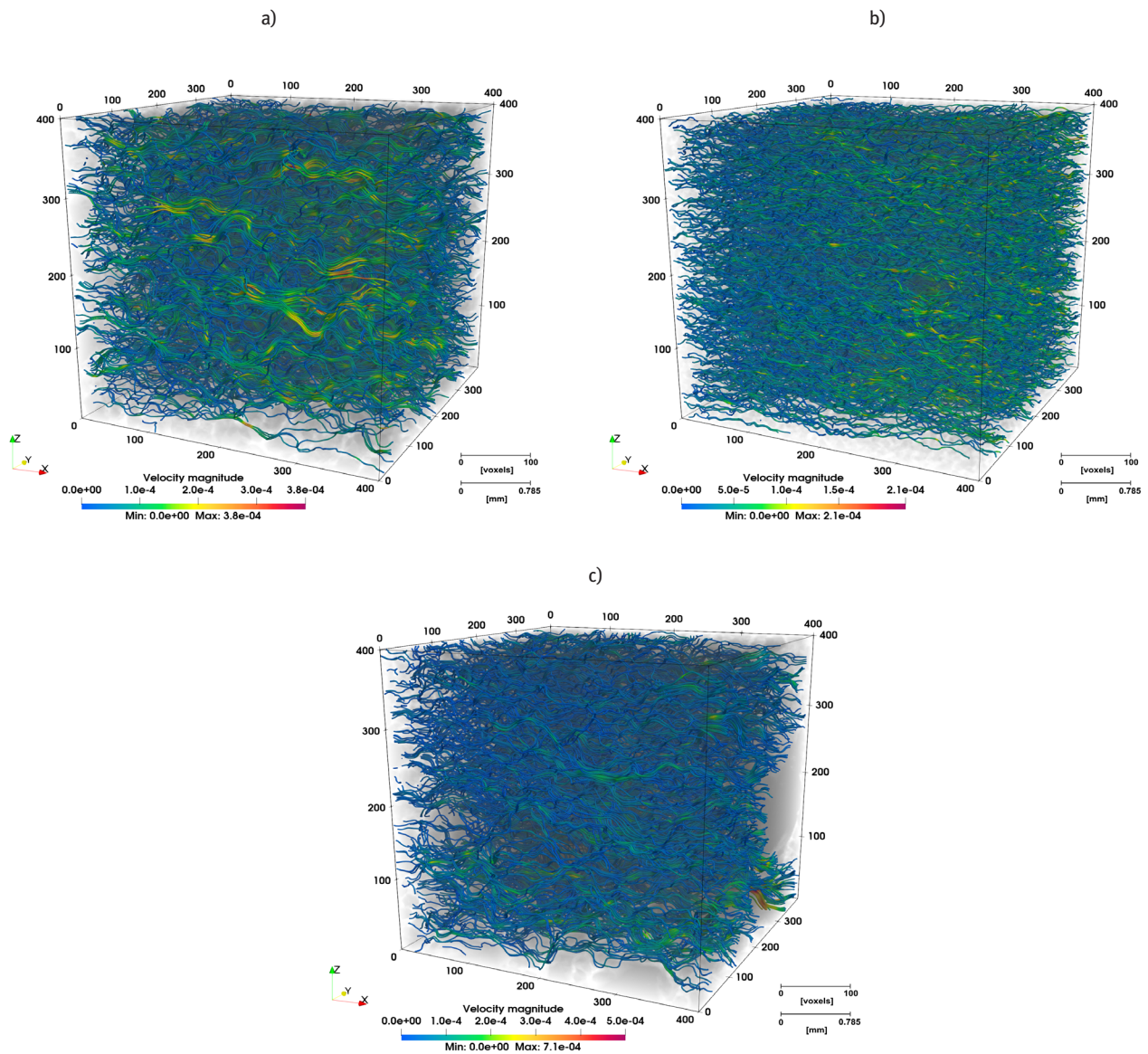| Sample no.	Sample name	VOI size	Porosity derived from image data	Permeability	Hydraulic conductivity at 10ºC
		[vx]	φ_{img} [-]	k [µm²]	K [m/s]
1	Fine sand	400³	0.365	23.489	1.758E-4
		600³	0.364	17.567	1.317E-4
2	Fine sand with lignite	400³	0.511	20.923	1.565E-4
		600³	0.511	23.193	1.736E-4
3	Medium sand	400³	0.309	16.778	1.259E-4
		600³	0.317	15.396	1.151E-4

a)

b)

c)

Figure 13: Streamlines of flow calculated using LBM: a) sample 1, b) sample 2, and c) sample 3.
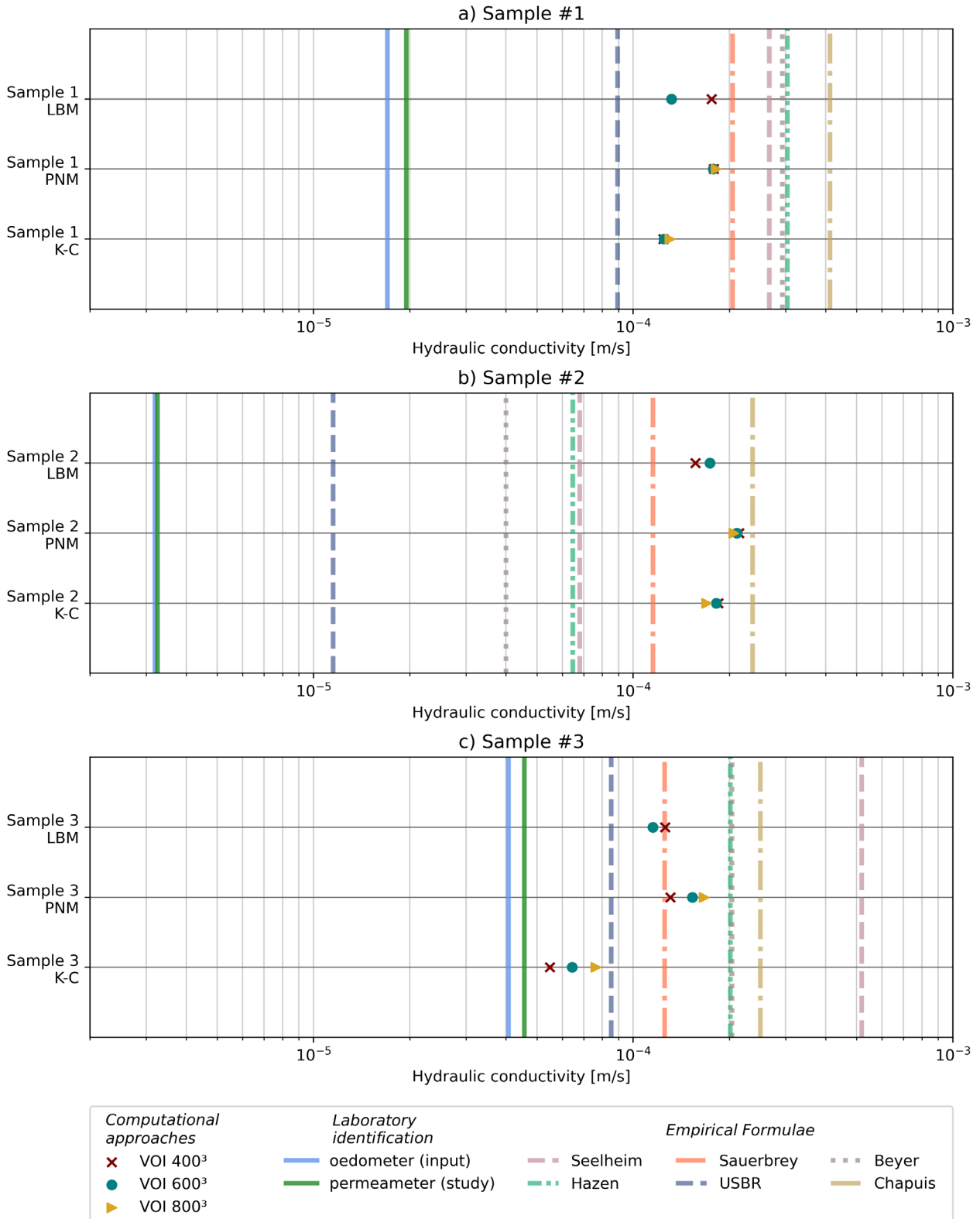
Figures 14: Calculated and measured hydraulic conductivities for a) sample 1, b) sample 2, and c) sample 3.

4 Discussion of results

For all three specimens, the hydraulic conductivity was assessed based on the analysis of 3D images obtained from micro-CT. Generally, for most VOI sizes chosen, derived data provided comparable results. They were summarized in Figure 14 for the individual samples and different VOI sizes, namely, 400^3, 600^3, and 800^3 [vx]. Vertical lines represent values obtained from empirical formulae and laboratory granulometric analysis, while solid blue and green lines depict conductivity obtained from test in oedometer and designed small-scale permeameter, respectively.

Applying empirical formulae to estimate soil hydraulic conductivity based on either the granulometric data or the described micro-CT-based procedure yielded a diverse range of results. Among different approaches, USBR formula stood out by providing a closest alignment to laboratory measurements by utilizing both the real and simulated grain size distributions as an input. The variation of results, depending on the equation used, emphasizes the necessity of considering multiple formulations to prevent misestimation of the conductivity.

Notably, for finer particle compositions, subtle deviations between the actual and estimated distribution of the grain sizes emerged primarily in the lower spectrum of the effective diameters. These differences were attributed to the aggregation of finer particles into larger entities during the processes of scanning and binarization. However, these distinctions did not hinder the curve alignment, as reflected in high values of the determination coefficient. In the case of sample 3 that exhibited a wider range of the grain sizes, the simulated curve became misaligned in the upper range of values. This issue was mitigated by utilizing larger VOI, suggesting the impact of the high REV size. Nonetheless, empirically derived permeability for this sample showed the closest agreement with values computed from laboratory granulometric analysis.

The results acquired with the Kozeny–Carman equation closely resembled the measurements for sample 3, while showing overestimation for samples 1 and 2. This might suggest that for the analyzed samples, the fine-side limit of validity has been approached. Content of organic material in sample 2 might also have contributed to the misestimation of its permeability.

Similar conclusions were made in accordance to the outcomes of pore-network and lattice-Boltzmann simulations. The highest similarity to the measured values was observed during analyses of sample 3, while the lowest value was observed in case of sample 2. The pore-network modeling approach was found to be the least accurate for all reviewed specimens possibly due to the high level of oversimplification of the microstructure.

Regarding the essential limitations of the methods employed in the study, the following issues are to be noted. Apparently, the scale effect remained a challenge that has not been fully mitigated. Even considering the largest VOI size that has been used for analysis, the numerical simulations were conducted on approximately 60% of the cross-sectional area of the scanned specimens. It has been shown that especially for sample 3, the accuracy of the results was influenced by the size of the VOI chosen. This underscores the importance of detailed representative-elementary volume (REV) analysis and finds the optimal scanning resolution prior to actual calculation of the soil hydraulic properties for a reliable and effective outcome.

The discrepancies between the estimated and measured values might have been also caused by the fact that most single-phase transport simulations do not take into account the effects present at the solid phase–fluid interface, which become increasingly significant in media with small-sized pores. That possibility gained credibility, considering that the outcomes of the simulations within sample 3, characterized by the overall thickest pores, exhibit closest alignment with the measured results. Another factor to be considered is the relationship between the permeability of the soil, applied external pressure, and its compaction. For a meaningful comparison of methodologies, it is crucial that the conditions of both laboratory measurements and scanning align in terms of the porosity of the sample in consideration. The potential impact of filter clogging and specimen swelling is also a consideration that cannot be dismissed when dealing with silty and organically contaminated soils.

4.1 Benchmark of the employed methods

Computational efficiency is a matter of great importance in investigation of soil properties from reconstructed images, especially considering large datasets to process. The minimal and maximal times of computation observed for different methods have been provided in Table S1 in supplementary materials, as well as the overview of the computational platform specifications.

The computation time varied among individual samples, with sample 3 generally requiring the shortest calculation time, while sample 2 the longest. That can be attributed to the fact that these specimens represent opposite ends of the porosity and feature number spectrum. The pore-network-based simulation exhibited

the shortest computation time for all assessed VOI sizes, but it also showed the lowest overall accuracy. Interestingly, the computationally expensive lattice-Boltzmann method did not yield the most accurate results for the analyzed samples.

5 Summary and conclusions

The objective of the research was to assess different methodologies to determine the permeability of sandy soils. This involved analyses utilizing 3D microstructure images from micro-CT as well as the results from direct laboratory measurements of hydraulic conductivity. Three sand samples of different composition and grain size distribution were tested.

It was found that the image-based approximation tends to set upper bound of permeability estimation, while laboratory measurements mark the lower bound. The latter may actually underestimate hydraulic conductivity as apparent decrease in assessed conductivity of finer samples (1 and 2) over the subsequent tests and filter clogging were observed.

The custom-made permeameter was built so that exactly the same samples were tested in both approaches. After all, falling-head tests in the small-scale permeameter as well as in the conventional oedometer resulted in convergent values of hydraulic conductivity despite the variation in sample size. It follows that the comparison of test results on small-scale samples (typically used in micro-CT) with those used in standard laboratory investigations is justified for the sands considered.

The influence of the adopted VOI size was verified in the image-based approach. For samples 1 and 2 pore-network modeling, Kozeny–Carman equations and simulated sifting methods proved to be the least affected by the size of chosen VOI. The differences were greater for sample 3 containing the largest grains. This suggests that the condition of representativeness of the chosen VOI might not have been fulfilled for that particular specimen.

The benchmark analysis demonstrated that pore-network modeling was the most time-efficient computational method reflecting actual pore microstructure morphology while not requiring so much time and computational resources as the lattice-Boltzmann method. At the same time, both the Kozeny–Carman and simulated sifting approaches presented a balanced computational efficiency. Furthermore, utilizing modern imaging techniques made the Kozeny–Carman equation a practical tool for evaluating the hydraulic

properties of porous media. It stems from solid theoretical foundations and, at the same time, microstructure morphology obtained from micro-CT allows accurate determination of parameters needed.

Summing up, microstructure image-based methods utilized in this study offer a viable addition to conventional permeability estimation approaches and a promising alternative to laboratory testing. To bridge the existing gaps between these two areas, future research will focus on representative elementary volume size determination and adoption of optimal resolution. This represents the planned direction for further investigations as a follow-up to this study.

References

[1] Ahrens, J., Geveci, B., & Law, C. (2005). ParaView: An End-User Tool for Large-Data Visualization. In *Visualization Handbook* (pp. 717–731). Elsevier. https://doi.org/10.1016/B978-012387582-2/50038-1

[2] Beyer, W. (1964). Zur Bestimmung der Wasserdurchlässigkeit von Kiesen und Sanden aus der Kornverteilungskurve. *Wasserwirtschaft Wassertechnik*, *14*(6), 165–168.

[3] Blott, S. J., & Pye, K. (2007). Particle shape: A review and new methods of characterization and classification. *Sedimentology*, *55*, 31–63. https://doi.org/10.1111/j.1365-3091.2007.00892.x

[4] Blunt, M. J., Bijeljic, B., Dong, H., Gharbi, O., Iglauer, S., Mostaghimi, P., Paluszny, A., & Pentland, C. (2013). Pore-scale imaging and modelling. *Advances in Water Resources*, *51*, 197–216. https://doi.org/10.1016/j.advwatres.2012.03.003

[5] Carman, P. C. (1937). Fluid Flow through Granular Beds. *AIChE*, *15*.

[6] Carman, P. C. (1956). *Flow of Gases through Porous Media*. Academic Press Inc.

[7] Carrier, W. D. (2003). Goodbye, Hazen; Hello, Kozeny-Carman. *Journal of Geotechnical and Geoenvironmental Engineering*, *129*(11), 1054–1056. https://doi.org/10.1061/(ASCE)1090-0241(2003)129:11(1054)

[8] Chapuis, R. P., Dallaire, V., Marcotte, D., Chouteau, M., Acevedo, N., & Gagnon, F. (2005). Evaluating the hydraulic conductivity at three different scales within an unconfined sand aquifer at Lachenaie, Quebec. *Canadian Geotechnical Journal*, *42*(4), 1212–1220. https://doi.org/10.1139/t05-045

[9] Dong, H., & Blunt, M. J. (2009). Pore-network extraction from micro-computerized-tomography images. *Physical Review E*, *80*(3), 036307. https://doi.org/10.1103/PhysRevE.80.036307

[10] Dullien, F. A. L. (1979). Single-Phase Transport Phenomena in Porous Media. In *Porous Media* (pp. 157–234). Elsevier. https://doi.org/10.1016/B978-0-12-223650-1.50009-7

[11] Fatt, I. (1956). The Network Model of Porous Media. *Transactions of the AIME*, *207*(01), 144–181. https://doi.org/10.2118/574-G

[12] Feldkamp, L. A., Davis, L. C., & Kress, J. W. (1984). Practical cone-beam algorithm. *Journal of the Optical Society of America A*, *1*(6), 612. https://doi.org/10.1364/JOSAA.1.000612

[13] Feng, J., Teng, Q., He, X., Qing, L., & Li, Y. (2018). Reconstruction of three-dimensional heterogeneous media from a single two-dimensional section via co-occurrence correlation function. *Computational Materials Science*, *144*, 181–192. https://doi.org/10.1016/j.commatsci.2017.11.030

[14] Frisch, U., Hasslacher, B., & Pomeau, Y. (1986). Lattice-Gas Automata for the Navier-Stokes Equation. *Physical Review Letters*, *56*(14), 1505–1508. https://doi.org/10.1103/PhysRevLett.56.1505

[15] Gostick, J. (2017). Versatile and efficient pore network extraction method using marker-based watershed segmentation. *Physical Review E*, *96*(2), 023307. https://doi.org/10.1103/PhysRevE.96.023307

[16] Gostick, J., Aghighi, M., Hinebaugh, J., Tranter, T., Hoeh, M. A., Day, H., Spellacy, B., Sharqawy, M. H., Bazylak, A., Burns, A., Lehnert, W., & Putz, A. (2016). OpenPNM: A Pore Network Modeling Package. *Computing in Science & Engineering*, *18*(4), 60–74. https://doi.org/10.1109/MCSE.2016.49

[17] Gostick, J., Khan, Z., Tranter, T., Kok, M., Agnaou, M., Sadeghi, M., & Jervis, R. (2019). PoreSpy: A Python Toolkit for Quantitative Analysis of Porous Media Images. *Journal of Open Source Software*, *4*(37), 1296. https://doi.org/10.21105/joss.01296

[18] Hazen, A. (1911). Discussion: Dams on sand foundations. *Transactions, American Society of Civil Engineers*, *73*(11).

[19] Hu, Y., Li, T.-M., Anderson, L., Ragan-Kelley, J., & Durand, F. (2019). Taichi: A language for high-performance computation on spatially sparse data structures. *ACM Transactions on Graphics*, *38*(6), 201:1-201:16. https://doi.org/10.1145/3355089.3356506

[20] Hussain, F., & Nabi, G. (2016). Empirical Formulae Evaluation for Hydraulic Conductivity Determination Based on Grain Size Analysis. *Pyrex Journal of Research in Environmental Studies*, *3*, 26–32.

[21] Kaviany, M. (1995). *Principles of Heat Transfer in Porous Media*. Springer New York. https://doi.org/10.1007/978-1-4612-4254-3

[22] Kelokaski, M., Siitari-Kauppi, M., Sardini, P., Möri, A., & Hellmuth, K.-H. (2006). Characterisation of pore space geometry by 14C-PMMA impregnation—Development work for in situ studies. *Journal of Geochemical Exploration*, *90*(1–2), 45–52. https://doi.org/10.1016/j.gexplo.2005.09.005

[23] Kozeny, J. (1927). Ueber kapillare Leitung des Wassers im Boden. *Sitzungsber Akad. Wiss.*, *136(2a)*, 271–306.

[24] Krüger, T., Kusumaatmaja, H., Kuzmin, A., Shardt, O., Silva, G., & Viggen, E. M. (2017). *The Lattice Boltzmann Method: Principles and Practice*. Springer International Publishing. https://doi.org/10.1007/978-3-319-44649-3

[25] Lindquist, W. B., & Venkatarangan, A. (1999). Investigating 3D geometry of porous media from high resolution images. *Physics and Chemistry of the Earth, Part A: Solid Earth and Geodesy*, *24*(7), 593–599. https://doi.org/10.1016/S1464-1895(99)00085-X

[26] *OpenCV 4.6.0.* (n.d.). https://docs.opencv.org/4.6.0/

[27] Pap, M., & Mahler, A. (2018). Comparison of Different Empirical Correlations to Estimate Permeability Coefficient of Quaternary Danube Soils. *Periodica Polytechnica Civil Engineering*. https://doi.org/10.3311/PPci.13108

[28] Říha, J., Petrula, L., Hala, M., & Alhasan, Z. (2018). Assessment of empirical formulae for determining the hydraulic conductivity of glass beads. *Journal of Hydrology and Hydromechanics*, *66*(3), 337–347. https://doi.org/10.2478/johh-2018-0021

[29] Sauerbrey, I. I. (1932). On the Problem and Determination of the Permeability Coefficient. *Proceedings VNIIG, 3–5.*

[30] Seelheim, F. (1880). Methoden zur Bestimmung der Durchlässigkeit des Bodens. *Zeitschrift Für Analytische Chemie*, *19*(1), 387–418. https://doi.org/10.1007/BF01341054

[31] Tranter, T. G., Kok, M. D. R., Lam, M., & Gostick, J. (2019). pytrax: A simple and efficient random walk implementation for calculating the directional tortuosity of images. *SoftwareX*, *10*, 100277. https://doi.org/10.1016/j.softx.2019.100277

[32] Valsecchi, A., Damas, S., Tubilleja, C., & Arechalde, J. (2020). Stochastic reconstruction of 3D porous media from 2D images using generative adversarial networks. *Neurocomputing*, *399*, 227–236. https://doi.org/10.1016/j.neucom.2019.12.040

[33] Verruijt, A. (1970). *Theory of Groundwater Flow*. Macmillan Education UK. https://doi.org/10.1007/978-1-349-00175-0

[34] Vukovic, M., & Soro, A. (1992). *Determination of Hydraulic Conductivity of Porous Media from Grain-size Composition*. Water Resources Publications. https://books.google.pl/books?id=q_FOAQAAIAAJ

[35] Wyllie, M. R. J., & Rose, W. D. (1950). Application of the Kozeny Equation to Consolidated Porous Media. *Nature*, *165*(4207), 972–972. https://doi.org/10.1038/165972a0

[36] Yang, J., Xu, Y., & Yang, L. (2022). Taichi-LBM3D: A Single-Phase and Multiphase Lattice Boltzmann Solver on Cross-Platform Multicore CPU/GPUs. *Fluids*, *7*(8), Article 8. https://doi.org/10.3390/fluids7080270

[37] Živković, P., Burečić Šafran, M., & Kovačević Zelić, B. (2021). Comparison of measured and estimated permeability for artificially prepared coarse-grained soil samples. *Rudarsko-Geološko-Naftni Zbornik*, *36*(3), 167–178. https://doi.org/10.17794/rgn.2021.3.12

Supplementary Material   **Open Access**

Bartłomiej Bodak*, Maciej Sobótka

Supplementary Material: Insights Into Estimation of Sand Permeability: From Empirical Relations to Microstructure-based Methods

Table S1: Computational efficiency of the methods presented.

Method	VOI size	Minimal measured total computation time	Maximal measured total computation time	Computational platform
	[vx]	t_{min}	t_{max}	CPU, CPU clock, RAM size and type, GPU and VRAM size (if applicable)
Simulated sifting	400^3	9 min	11 min	AMD Ryzen™ 7 5800H @ 3.2 GHz, 32 GB DDR4 RAM
	600^3	34 min	36 min	
	800^3	81 min	95 min	
Kozeny–Carman	400^3	5 min	7 min	
	600^3	13 min	13 min	
	800^3	32 min	58 min	
Pore-network	400^3	2 min	5 min	
	600^3	7 min	18 min	
	800^3	18 min	42 min	
Lattice Boltzmann CPU	400^3	22 h 31 min	34 h 35 min	2 x Intel® Xeon® E5-2687W @ 3.1GHz, 128 GB DDR3 RAM
	600^3	75 h 58 min	115 h 18m	
Lattice Boltzmann GPU	400^3	69 min	105 min	AMD Ryzen™ 9 5950x @ 3.4 GHz, 64 GB DDR4 RAM, NVIDIA RTX™3090 24 GB VRAM